Journal of Hazardous Materials 476 (2024) 134928

Contents lists available at ScienceDirect

Journal of Hazardous Materials

journal homepage: www.elsevier.com/locate/jhazmat

Identification and quantification protocol of hazardous-metal bearing minerals: Ni in serpentinite rocks from Valmalenco (Sondrio, Central Alps, Northern Italy)

Riccardo Fantini [a,*], Mattia Sisti [a], Rossella Arletti [a], Daniele Malferrari [a], Maria Cristina Gamberini [b], Mauro Zapparoli [c], Filippo Da Val [d], Alessandro Cavallo [e], Alessandro Francesco Gualtieri [a]

[a] Chemical and Geological Sciences Department, University of Modena and Reggio Emilia, Via G. Campi 103, Modena 41125, Italy
[b] Department of Life Sciences, University of Modena and Reggio Emilia, Via G. Campi 103, Modena 41125, Italy
[c] Centro Interdipartimentale Grandi Strumenti (CIGS), University of Modena and Reggio Emilia, Via G. Campi 213/A, Modena 41125, Italy
[d] Alfa Solutions S.p.A. Viale B. Ramazzini, 39D, Reggio Emilia 42124, Italy
[e] Department of Earth and Environmental Sciences, University of Milano-Bicocca, Piazza della Scienza 1, Milano 20126, Italy

HIGHLIGHTS

- Potential eco-health risk: Ni in serpentinites and their by-products.
- New protocol: i) measure bulk Ni; ii) quantify Ni minerals; iii) compare results.
- Case study: commercial serpentinites of Valmalenco (Sondrio, Central Alps, Italy).
- Bulk Ni: 1390-1750 mg/kg; Ni from minerals: 1924-1761 mg/kg.
- The protocol for Ni is robust.

GRAPHICAL ABSTRACT

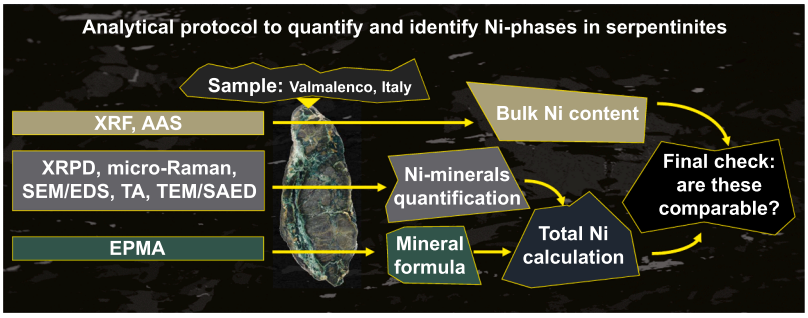

ARTICLE INFO

Keywords:
Serpentinite
Nickel
Hazardous waste

ABSTRACT

Serpentinite is a widespread rock type used worldwide as building material. Heavy metals like Ni in both the serpentinite products and serpentinite mining wastes pose potential environmental and health issues. This work devises an analytical protocol to identify and quantify the Ni speciation in the mineralogical matrix, through: i) bulk Ni quantification; ii) quantitative mineralogical and chemical analysis of each Ni-rich mineral; iii)

Abbreviations: AAS, atomic absorption spectroscopy; atg, antigorite; awr, awaruite; BF-STEM, bright field scanning transmission electron microscopy; brc, brucite; cpx, clinopyroxene; DTG, first derivative of TGA; EDS, energy dispersive X-ray spectroscopy; EPMA, electron probe microanalysis; HAADF-STEM, high-angle-annular-dark-field scanning transmission electron microscopy; hzl, heazlewoodite; ICP-MS, inductively coupled plasma-mass spectrometry; mgn, magnetite; MSEGA, mass spectrometry of evolved gasses; NOA, naturally occurring asbestos; ol, olivine; PCOM, phase-contrast optical microscopy; PLOM, polarized light optical microscopy; pnt, pentlandite; RTMS, real time multiple strip detector; SEM, scanning electron microscopy; TA, thermal analysis; TEM, transmission electron microscopy; TGA, thermogravimetric analysis; VG, "Verde Giada"; VV, "Verde Vittoria"; WDS, wavelength dispersion spectrometry; XRF, X-ray fluorescence spectrometry; XRPD, X-ray powder diffraction.

* Corresponding author.
E-mail address: riccardo.fantini1@unimore.itri (R. Fantini).

https://doi.org/10.1016/j.jhazmat.2024.134928
Received 3 February 2024; Received in revised form 7 June 2024; Accepted 13 June 2024
Available online 14 June 2024

X-ray powder diffraction
Valmalenco (Northern Italy)

comparison of bulk analysis results with the sum of each contribution from the Ni-rich minerals. As case study, two commercial serpentinites “Verde Giada” (VG) and “Verde Vittoria” (VV) from Valmalenco (Northern Italy) were analysed by ICP-MS, XRPD, TGA–MSEGA, SEM, TEM, EPMA, and micro-Raman spectroscopy. The bulk Ni content is 1500–1750 mg/kg and 1390–1620 mg/kg for VG and VV, respectively. The major minerals from XRPD and EPMA (antigorite, olivine, pyroxene, magnetite, brucite) account for 1094 and 1291 mg/kg of Ni for VG and VV, respectively. SEM/TEM and EPMA highlighted the presence of minor chrysotile, pentlandite, heazlewoodite, awaruite, rising the computed Ni to 1924 and 1761 mg/kg for VG and VV, in good agreement with bulk ICP-MS. This protocol provides robust results and can thus enhance the exposure assessment of Ni and eventually other naturally occurring hazardous metals.

1. Introduction

Serpentinite is a *green colour stone* characterized by one or more serpentine group minerals (namely antigorite, lizardite, and chrysotile) with a frequent texture and structures that resemble the skin of a serpent [1]. Serpentinites are ubiquitous ultramafic metamorphic rocks, mostly deriving from the hydrolization/hydration of peridotites occurring in ophiolitic and sub-continental mantle complexes [2,3]. The use of these rocks as building materials dates back to ancient times and there are numerous examples of past and actual uses of the serpentinites as building stones worldwide (see for example India, Italy, Pakistan, Spain and United States to quote the most remarkable ones reported by [4]). Due to their greenish appearance, serpentinites are often referred to as “*pietre verdi*" (literally ”green stones”) in the Italian market of ornamental stones.

One of the most important serpentinite mining area in Italy is Valmalenco (Sondrio, Central Alps, Northern Italy) where building stones have been extracted since the XI century, used in slabs for roofing and still exported today in the global market [2]. In Valmalenco, there are two major commercial varieties: schistose or “slaty” (“Serpentino-scisto”) and "massive" serpentinite (“Serpentino Massiccio”) [2,5]. These serpentinite rocks contain a mineralogical assemblage characterized by various generations of antigorite, olivine, clinopyroxene, chlorite, magnetite and minor chromite, Fe–Ni alloys, Fe–Ni sulphides and Ti-clinohumite. The antigorite amount is variable, and the spectrum ranges from completely serpentinised rocks to serpentinites with considerable amounts (>40 % modal) of olivine and pyroxene. Other observed accessory minerals are represented by ilmenite, alloys (e.g. awaruite Ni_3Fe) and native Cu [6,7,2]. Moreover, native nickel-iron and bravoite may also occur [8].

There are well known environmental issues connected to the mining activity of serpentinites widely described in the literature with reference to the Valmalenco area [2]. The most important hazard is certainly represented by NOA (*naturally occurring asbestos*) with chrysotile commonly found within the rock mass along fractures and cracks [5,7] and amphibole asbestos fibres like tremolite more rarely found as accessory phases in some valley *green stones* [9]. The mining activity itself and the processing of the waste material represent the second environmental concern. About 45–50 % of the *tout-venant* of the raw rock is lost in the quarry in the form of shapeless blocks and to date there are no significant recycling applications of the serpentinite waste products [5]. The serpentine tailings from asbestos-containing materials are a potential health hazard for the population living in the surrounding areas, as it was shown for the asbestos mines in Quebec (Canada) [10-12]. A third emerging concern regards the presence of heavy metals like Ni and Cr in both the serpentinite products and the mining wastes that can be eventually leached and released in the environment with potential health risk [13-15]. It is well known that paedogenetic processes involving serpentinites lead to soils characterized by high contents of asbestos minerals [16,17] and of metals like Cr, Co, and Ni derived directly from the parent rock [18,19,14], with total content that may reach up to 2000 mg/kg [20]. Moreover, it must be stressed, that particular effort is ongoing to study potentially toxic elements hosted in asbestos elongate mineral particles as one of the factors that determines their toxic/pathogenic effects (e.g. [21]). The determination of the content of heavy metals and the nature of the mineralogical matrix that accommodates those metals in serpentinite rocks and their mining wastes allow to assess their toxicity and carcinogenicity potential. In the case of Ni, it is important to evaluate the presence and concentration of bunsenite, NiO, a regulated known carcinogen. Knowing the nature of mineral phases hosting heavy metals also permits to classify the hazardous serpentinite waste with the existing national regulations and addresses the correct disposal action. Moreover, the risk assessment associated to the occurrence and speciation of heavy metals like Ni and Cr is of paramount importance in every industrial processing associated to this material (e.g. laser cleaning in [22]).

In this paper, we devised an analytical protocol for the qualitative and quantitative determination of Ni in serpentinite rocks using a suite of complementary experimental techniques with the aim to identify the nature of the Ni-containing phases and their quantification for the assessment of the potential hazardousness. To this aim, we selected the Italian Valmalenco "massive" serpentinite quarries of “Verde Vittoria” and “Verde Giada” as case studies. This study is of paramount importance for defining the toxicity and carcinogenicity potential of Ni-containing substances, as well as for classifying the hazardous wastes resulting from the mining and processing of serpentinites. Here, we have identified each occurrence of Ni in these serpentinites, not only the species associated to asbestos minerals that, indeed, represent a really minor component of the studied samples.

2. Materials and methods

2.1. Valmalenco geology and mining activity

Valmalenco is located in the Lombardy region, about 100 km N of Milan and close to the Italy-Switzerland border (Fig. 1). It is one of the most important side valleys of Valtellina and is located on the hydrographic right of the Adda River, covering an area of about 315 km^2 and a length of nearly 25 km. It is situated in the Alps, which are one of Europe’s most important mountain ranges, and their formation is associated with the opening of the Atlantic Ocean during the Cretaceous period. In Valmalenco, the geological-structural setting appears to be particularly complex [23], characterized by the following tectonic units, from bottom to top: upper Penninic (Suretta, Forno and Malenco nappes; the word nappe generally indicates an overthrust rock mass of major dimension transported horizontally) and lower Austroalpine (Margna, Sella, Bernina, Campo and Grosina-Tonale nappes). Valmalenco is home to one of the largest ultramafic bodies in the Alps: the Malenco unit (a subcontinental mantle fragment, preserving the Permian crust-mantle transition), which is then associated with a well-preserved Jurassic--Cretaceous related oceanic floor succession, the Forno unit (Münterer and Hermann, 1996; [24]). These tectonic units are placed between the nappes derived from the Adriatic microplate and the European plate. The Malenco nappe and the basement of the Margna nappe represent the pre-Alpine lithosphere of the Adria plate; both units are cut by the Permian Fedoz Gabbro [25,26]. The Malenco nappe consists mainly of serpentinites, serpentinized peridotites, and subordinate spinel lherzolites, dunites, garnet clinopyroxenites, and harzburgites. In the western

Valmalenco area the nappe pile is crosscut by the Oligocene Bergell and Triangia intrusives (mainly tonalites and granodiorites), with the development of a massive metamorphic contact aureole [23]. The structural evolution of the area is also very complex, characterized by three main deformational and metamorphic events [24]; in later phases of brittle character, of neo- and post-alpine age, characterized by circulation of hydrothermal fluids, there is the development of metric to decametric steatite (impure talc) lodes and chrysotile veins. The wide variety of lithologies and the tectono-metamorphic evolution of the area have made it very interesting from an extractive point of view: several serpentinite quarries (dimension stone, schistose and "massive" varieties), a large underground mine of steatite (Brusada-Ponticelli mine), as well as an underground soapstone (chlorite-schist) quarry are currently active. A valuable long-fibre chrysotile was also mined until the 1950s. More generally, the Valmalenco area was subject to chrysotile asbestos mining from the XIX century until 1975 (e.g. [7]). There are also numerous historical records of mining activities for white talc, various types of soapstone, Fe ores, and sulphides of Cu and Zn.

2.2. Sample description

Two representative samples of massive serpentinites “Verde Giada” (VG) and “Verde Vittoria” (VV) were collected at the Chiuro (Sondrio, Italy) plant of the Serpentino e Graniti Company, as rock chips of raw and semi-finished products, and were first reduced by crushing (hammer on anvil). Thus, the two samples used for analyses were provided in the form of fragments of 5–10 cm (Fig. 2).

2.3. The proposed analytical protocol

The objective of this section is to devise an analytical protocol for the identification and quantification of each mineral phase hosting Ni as major or trace element. The protocol (Fig. 3) is characterized by three main analytical paths: the first represent the independent quantification of bulk Ni content; the second and third paths are complementary and aim the identification of all the mineral phases present in the sample,

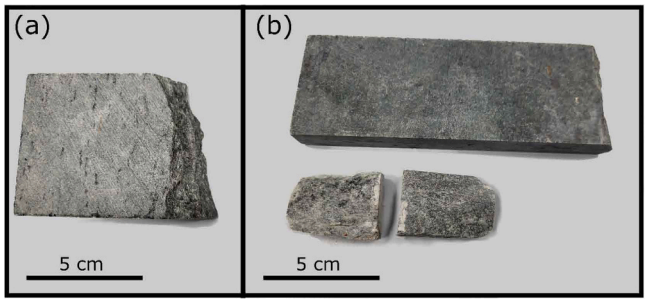

Fig. 2. Pictures of: (a) Verde Giada, VG; (b) Verde Vittoria, VV.

their accurate chemical analysis (possibly including trace elements), and finally the quantification of each Ni-containing phase. Concerning this last goal, path (2) directly provide the contribution of mineral phases quantified by X-ray powder diffraction (XRPD) to total Ni content (also as traces), while path (3) allow to quantify minor or trace mineral phases in which Ni represent one of the major constituents (e.g. Ni sulphides below 1 wt% in the sample). Some of the suggested analytical techniques (e.g. X-ray fluorescence spectrometry, XRF, and Atomic Absorption Spectroscopy, AAS) may be redundant and, depending on the case under study, they can serve as alternatives to each other. However, each technique provides different and complementary information (see **Table 1S** of Supplementary Material for a comparison). Some of this consideration will be presented concerning the case study of this paper.

The protocol of Fig. 3 was applied to determine the nature and content of Ni in the Valmalenco serpentinite samples VG and VV. Concerning the analytical path (1), the total content of Ni (mg/kg) of a sample is usually determined by inductively coupled plasma-mass spectrometry (ICP-MS), XRF or AAS; nevertheless, these methods do not provide information about the nature (i.e., chemical speciation) of the Ni-containing phases. As already pointed out in the introduction, the identification of the Ni containing mineral phase is of paramount importance to assure safety in the serpentinite dressing plants (e.g.

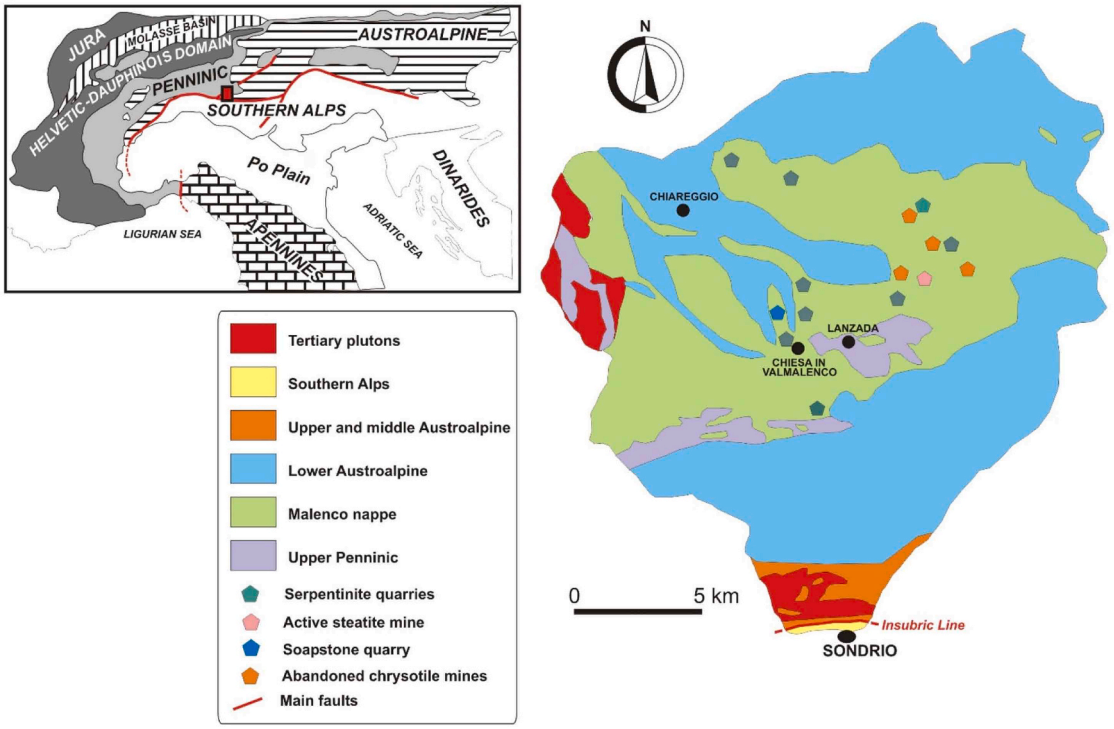

Fig. 1. Main structural domains of the Alps; the location of Valmalenco is indicated in the box and simplified geological sketch map of Valmalenco; major active and disused mining and quarrying activities (serpentinite, steatite, soapstone, chrysotile asbestos) are indicated. Colours in the online version (modified from [2]).

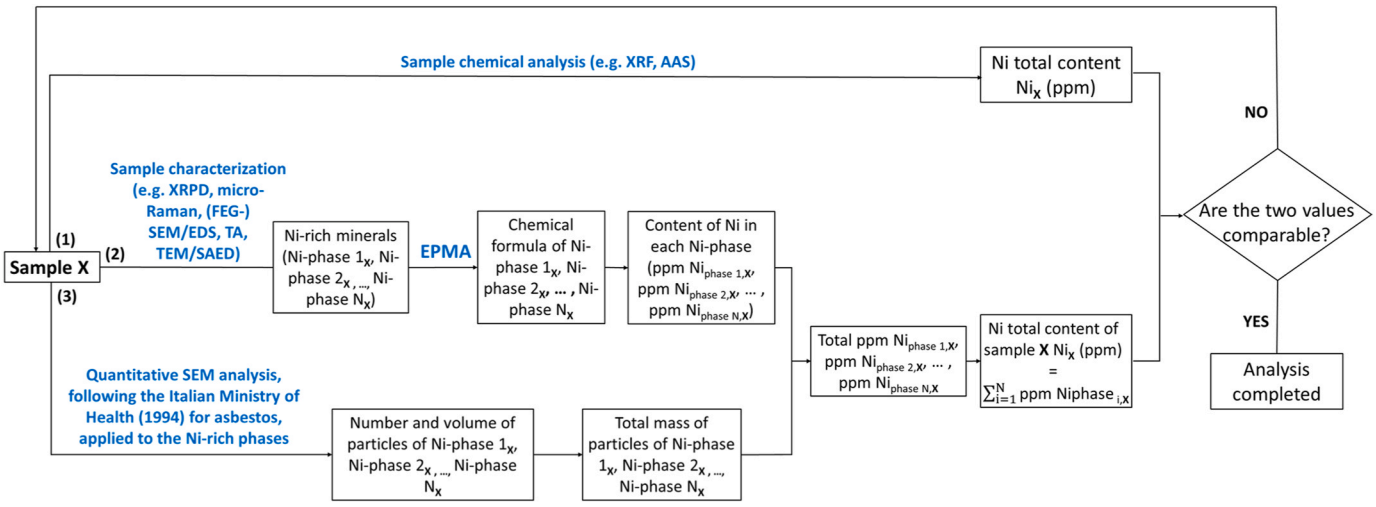

Fig. 3. Flow chart of the analytical protocol used in this work to determine the nature and content of Ni in the Valmalenco serpentinite samples VG and VV (see the text for details).

during laser cleaning, [22]) and properly classify the hazardous waste derived from these materials within the frame of the existing national regulations and address the correct disposal action.

Concerning path (2), a suite of bulk experimental techniques including XRPD, thermal analyses coupled with evolved gasses analyses (TGA–MSEGA), micro-Raman, scanning electron microscopy with energy dispersive X-ray spectroscopy (SEM/EDS), transmission electron microscopy (TEM) were used to assess the nature of mineral phases in the specimens, particularly focusing on the Ni-containing minerals. Moreover, electron Probe microanalysis (EPMA) permitted to collect quantitative chemical data of each mineral phase, with information on trace elements. This permitted the calculation of the chemical formula of each Ni-containing mineral in the samples.

As already mentioned, the analytical path (3) is particularly suited to quantify Ni-rich phases (e.g. alloys or sulphides) not detected by XRPD due to their low content in the specimens. For counting the Ni-rich minerals (Ni-phase 1, Ni-phase 2, ..., Ni-phase n) in both VG and VV samples, we applied the quantitative SEM analysis protocol used for the determination of asbestos minerals in massive samples, according with Italian Minister Decree 06.09.94 [27]. The size (and volume) of each Ni-bearing phase *i* was also measured. The concentration C (in mg/kg) of the Ni-phase *i* can be calculated using the equation below:

$$C_{Ni-phase\,i} = \frac{A \times w_{Ni-phase\,i}}{n \times a \times W} \times 10^6$$

with A = filter surface (mm^2); $w_{Ni\text{-}phase\ i}$ = total weight of counted Ni-phase *i* (mg) using the proper ideal value of the density of the Ni-phase *i* (g/cm^3); n = number of analysed fields; a = area of the fields (mm^2); W = weight of the sample on the filter (mg).

The concentration (wt%) of each Ni-containing mineral (Ni-phase 1, Ni-phase 2, ..., Ni-phase n) in the samples (both those quantified by XRPD and by SEM) was rescaled with respect to the content of Ni in their chemical formula, as determined by EPMA, to obtain the total Ni content (mg/kg) carried by each Ni-containing mineral in the samples. The sum of all these weights yields total content of Ni in the samples Ni$_X$ (wt%) to be compared to the values measured using the bulk methods. For simplicity in data management and processing, the adopted calculation setup overturned the process by calculating directly the Ni mass deriving from each counted object in the explored area and finally rescaling the Ni content to the sample with, conceptually, the same mathematical process of the equation above.

2.4. X-ray fluorescence spectrometry (XRF)

To perform XRF analysis, rock fragments of 5–10 cm were reduced mechanically below 0.5 cm and then finely ground by a Fritsch Pulverisette vibrating cup mill, equipped with an agate milling vessel. XRF pellets were then prepared by mixing 2.7 g of sample with 0.27 g of wax and 6 g of H_3BO_3 as a binder, and finally pressing the mixture at 15 tons into aluminum molds with a diameter of 40 mm. Data collection was performed by a Zetium wavelength-dispersive XRF spectrometer (Malvern Panalytical), equipped with a Rh X-ray tube. Data treatment was performed by using calibration curves of 54 certified silicate standards.

2.5. Inductively coupled plasma-mass spectrometry (ICP-MS)

Both VG and VV specimens were preliminary analysed for bulk chemical composition and Ni content. Samples were prepared reducing mechanically the rock fragments from 5–10 cm down to 0.3 cm. Successively, the specimens were ground by wet-milling with an aluminous porcelain jar in isopropyl alcohol for 10 min. The obtained sludge was dried in oven and, after drying, an aliquot was further ground in an agate mortar. The obtained powders were finally mineralized using a mixture of superpure 65 % HNO_3 and 48 % HF, followed by hot digestion for 90 min in a DIGIPREP MS extractor. The digestion granted the full solubilisation of all mineral phases resulting in a water-clear solution. The bulk Ni content was then measured by ICP-MS using a Thermo Fisher Scientific instrument "iCAP TQe" equipped with an ESI Fast 4DX autosampler.

2.6. Quantitative phase analysis

For XRPD measurements, rock fragments of 5–10 cm were first reduced mechanically down to 0.3 cm, and finally ground in agate mortar down to obtain a mean grain size of 10 μm.

XRPD patterns of the VG and VV samples were then collected with the side loading technique on zero-background quartz sample holder at ambient conditions using a θ–θ Bragg-Brentano PANalytical 'XPert Pro Diffractometer (Cu Kα radiation) equipped with a real time multiple strip (RTMS) detector. Specific set-up conditions were: CuK_α radiation, 40 kV, 40 mA, range of the data collection = 5–80 °2θ, virtual counting time = 55 s/0.0167 °2θ step, ½° divergence slit, ½° anti-scatter slit, Ni filter on the primary beam, anti-scatter blade slit of 5 mm before the detector and 0.02 rad Soller slits on both the primary and diffracted beam. Preliminary qualitative phase analyses were performed using the *X'Pert High Score Plus* (v. 2.2c) software (PANalytical BV, Almelo, The

Netherlands). Rietveld phase analysis was performed using the GSAS package [28] and its graphical interface EXPGUI [29]. During the Rietveld refinement, the cell parameters were refined together with the coefficients of the function modelling the background (a 6 to 9-term Chebyshev polynomial) and of the pseudo-Voigt function modelling the profile function of the Bragg peaks. Preferred orientation for some crystalline phase was corrected using the March–Dollase algorithm [30]. Structural models for all the phases were taken from The American Mineralogist Crystal Structure Database (*minsocam.org/msa/crystal_database.html*).

2.7. Thermogravimetry coupled with evolved gasses analyses (TGA-MSEGA)

The same powder specimens of 1–10 μm used for XRPD measurement were employed for TGA. TGA was performed with a Seiko SSC 5200 thermal analyser coupled with a quadrupole mass spectrometer (ESS, GeneSys Quadstar 422) to detect gases released during thermal reactions (MSEGA). Gas sampling was performed using a preheated silicon capillary to prevent gas condensation. The experimental conditions were: heating rate: 20 °C/min; heating range: 25–1050 °C; TGA data measurement: every 0.5 s; purging gas: ultrapure helium with a flow rate of 100 μL/min. Mass analyses were performed in multiple-ion detection mode by measuring m/z ratios (i.e., the dimensionless ratio of the mass number m to the z-charge of an ion) 18, 30, 34, 44, 64 to detect the emission of H_2O, NO, H_2S, CO_2 and SO_2, respectively, using a secondary electron multiplier detector set at 900 V with integration time of 1 s on each measured m/z.

2.8. micro-Raman

Raman analysis is possibly the only technique capable of providing mineralogical identification for minor mineral phases that are not detected by XRPD. In fact, even EPMA (Section 2.10) does not unequivocally provide phase identification, particularly for non-perfectly stoichiometric compounds.

Samples for micro-Raman analyses were prepared by embedding several rock fragments of ~1 cm in resin discs of 1 in. The surface of the sample was subsequently polished using a lapping machine, progressively transitioning to finer abrasives until reaching a 1 μm abrasive.

The Raman analyses were conducted with a confocal micro-Raman LabRAM HR evolution (Horiba Jobin Yvon, Edison, NJ, United States), equipped with a red He-Ne laser at 532 nm (1 μm-size spot), notch filters to eliminate the exciter, detector CCD front illuminated open electrode multi-pin phased, with 1024 × 256 × 16 pixels, cooled by a Peltier system. Spectra were recorded in backscattering after focalization in several positions within a small area of the specimen (ca. 100 ×100 μm). The maximum laser power employed was 20 mW and the recording time for a good signal-to-noise ratio was 10 s for 50 accumulations. LabSpec6 was used for the spectra elaboration.

2.9. Scanning electron microscopy (SEM)

SEM served as preliminary technique to qualitatively check on both the resin-embedded specimens before EPMA analyses and later for the quantitative analyses (as described in Section 2.12).

The preliminary morphological observations and qualitative chemical determinations of the samples were performed using a Scanning Electron Microscope (SEM) JSM-6010PLUS/LA (JEOL, Hillsboro, OR, USA) equipped with an Energy Dispersive X-ray (EDS) microanalysis system (Oxford INCA-350). Images were primarily acquired in backscattered electron mode (BSE) to enhance compositional contrasts.

2.10. Electron probe microanalysis (EPMA)

The resin-embedded specimens used for the micro-Raman measurements were employed for EPMA analyses . The resin discs were metallized with carbon to make them conductive.

EPMA with quantitative wavelength dispersion spectrometry (WDS) microanalyses was then performed using a JEOL 8200 Super Probe with W hairpin type filament equipped with five wavelength-dispersive spectrometers. The analytical conditions for the electron beam were: accelerating voltage = 15 kV, beam current = 5 nA, beam diameter = 1 μm, counting time of 30 s for the peak and 10 s for the background for each element.

2.11. Transmission electron microscopy (TEM)

TEM experiments were performed using a Thermo Fisher Scientific Talos F200S G2 FEG-TEM instrument equipped with a CETA 16 M CMOS camera, STEM detectors, in HAADF (high-angle-annular-dark-field scanning transmission electron microscopy), ADF, ABF and BF-STEM (bright field scanning transmission electron microscopy) modes, and EELS with Gatan Enfinium SE/976 detector. The investigated materials were dispersed in distilled water. Subsequently, a drop of suspension was placed on a copper holder. Images were collected at 200 keV.

2.12. SEM quantitative determination protocol

Dimensional and chemical information of Ni-rich minerals was obtained using a FEG-SEM FEI Nova Nano-SEM 450, equipped with a Bruker XFlash-5010 EDS detector. Samples were prepared by first reducing mechanically the rock fragments of 5–10 cm below 1 cm and next by wet-milling with an aluminous porcelain jar in isopropyl alcohol for 10 min. The obtained sludge was dried in oven and, after drying, an aliquot was further ground in an agate mortar. Subsequently, the powder were suspended at a concentration of 0.5 mg/ml in ultrapure water with 0.1 % Aerosol OT surfactant. The suspension was kept under stirring and 0.5 ml were withdraw and filtered through a polycarbonate Millipore™ filter (25 mm of diameter, and 0.8 μm of porosity). Filters were then mounted on a conventional SEM stub and coated with gold.

The quantification of Ni-rich mineral individuals was performed observing 80 fields for both VV and VG, at a magnification of 3000x (field of 138 ×92 μm^2) in backscattered electron mode (BSE). In these conditions, 80 fields correspond to roughly 1 mm^2. Fields were chosen applying a regular grid with 0.7 mm shift horizontally and vertically, thus preventing overlaps (see Supplementary Material Fig. 1S). Any observed object was studied in detail and analysed by EDS to confirm and quantify the Ni content. EDS analysis was performed using the Phi-Rho-Z method with 50 s counting time. Then, the volume of the particle was estimated assuming equivalent cylinders, spheres, cubes, or cuboids, on shape basis. Effects of comminution were also considered during morphological observations [31].

Thanks to chemical data, any observed individual was attributed to a specific mineral phase, thus allowing total Ni estimation through volume, density, and sample preparation data (i.e. suspension density, filtered volume).

3. Results and discussion

The sections below follow the concept scheme of the flow chart reported in Fig. 3.

3.1. Samples' chemical analysis

The chemical analysis of bulk VG and VV samples from XRF is reported in Table 1a. Bulk Ni content is 1747 and 1533 mg/kg for VG and VV respectively. Accordingly, the determination of the bulk Ni content by ICP-MS analyses, repeated twice on both specimens, highlighted a slightly higher value in VG (1500–1750 mg/kg) compared to VV (1390–1620 mg/kg).

Table 1a
Bulk chemical analysis from XRF. Major elements reported as oxide wt% while trace elements are in mg/kg. Fe_2O_3 refers to total iron content. Loss on ignition (L.o.I.) is from TGA. Omitted elements/oxides were below detection limit.

Sample	VG	VV
Major oxides (wt%)		
SiO_2	39.55	38.02
Al_2O_3	1.18	0.88
Fe_2O_3	7.23	8.21
MnO	0.12	0.11
MgO	43.1	41.48
CaO	0.12	0.88
TiO_2	0.01	0.01
P_2O_5	0.02	0.02
L.o.I.	8.25	9.94
Trace elements (mg/kg)		
S	225	119
Cl	92	76
Sc	12	12
V	39	42
Cr	2562	3052
Co	100	88
Ni	1747	1533
Cu	6	10
Zn	38	38
Zr	10	16
Sn	5	-
Ba	13	13
Pb	2	4
La	8	8
Ce	25	29
Nd	5	6
Th	1	2

3.2. Samples' characterization

Table 1b shows the quantitative phase analysis of representative samples of VG and VV, determined from XRPD with the Rietveld method. Antigorite is the major phase in both the VG and VV samples with subordinate olivine, pyroxene and magnetite. Brucite is abundant in the VV sample but minor in the VG sample. Assuming that the average detection limit of the technique under the experimental conditions used is around 0.2–0.3 wt%, none of the following mineralogical phases were observed in the analysed powder patterns: amphiboles, apatite, awaruite, bunsenite, Ti-clinohumite, chrysotile, heazlewoodite, ilmenite, pentlandite, pyrrhotite, spinel/chromite.

The TGA and its first derivative (DTG) curves (Fig. 4a) of sample VV show four thermal events: (1) 25–200 °C (maximum reaction rate at 68 °C, mass loss of 0.18 wt%); (2) 315–425 °C (382 °C, 0.97 wt%); (3) 550–850 °C (781 °C, 8.34 wt%); (4) 850–930 °C (878 °C, 0.22 wt%). All the reactions involve the release of water only ($m/z = 18$, Fig.2Sa of Supplementary Material). The thermal behaviour of the VG sample (Fig. 4b, and Fig.2Sb of Supplementary Material) essentially parallels the previous one, and the same thermal reactions are identified; nevertheless, minor shifts in the thermal range of development of individual reactions and differences, sometimes more significant, in the mass change, can be observed: (1) at temperatures below 200 °C (maximum reaction rates at 40 and 70 °C, mass loss of 0. 28 wt%); (2) 315–435 °C (366 °C, 0.22 wt%); (3) 545–850 °C (778 °C, 7.20 wt%); (4) 850–930 °C (879 °C, 0.23 wt%).

Table 1b
Results of the quantitative phase analysis from XRPD data using the Rietveld method.

	VG	VV
Rietveld agreement indices*		
R_{wp} (%)	22.26	20.22
R_p (%)	16.11	14.56
χ^2	10.77	8.473
Phases** (wt%)		
antigorite	73.3(1)	72.8(1)
brucite	0.3(1)	5.1(1)
clinopyroxene	1.4(1)	5.2(1)
magnetite	2.6(1)	3.8(1)
olivine	22.4(1)	13.1(1)
Total	100	100

* The definition of the agreement indices is taken from [28];
** The following structure models were used: antigorite from Capitani and Mellini [32]; brucite from Hofmeister and Platen [33]; diopside from Cameron et al. [34]; magnetite from Yoshida and Iida [35]; forsterite from Birle et al. [36].

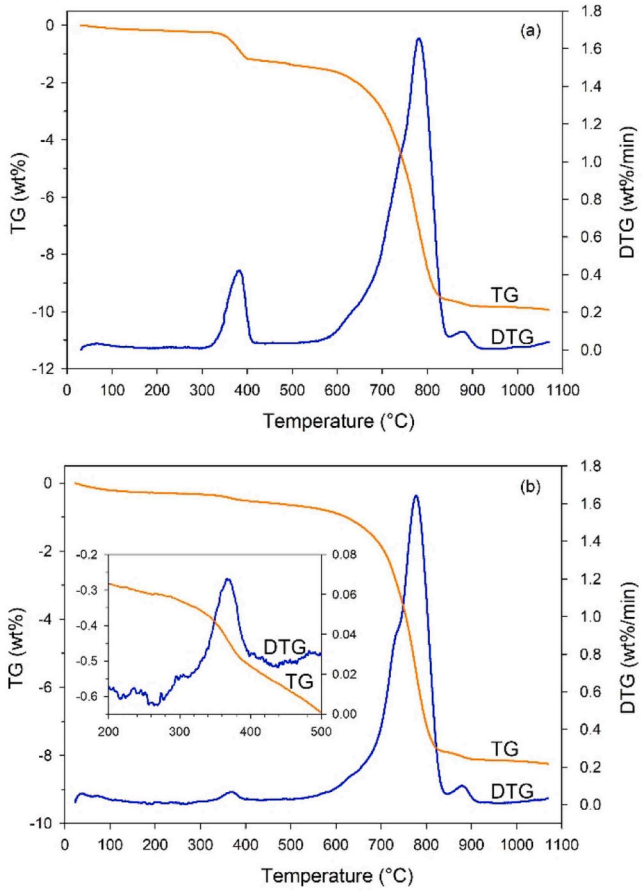

Fig. 4. TG (yellow line) and DTG (blue line) curves of sample VV (a) and VG (b). The magnification inside (b) better highlights the loss of water due to thermal decomposition of brucite.

Concerning the reaction sequence, reaction (1) can be ascribed to the removal of more or less strongly bound hydration water [37,38]. Reactions (2), best highlighted for the VG sample in the magnification within Fig. 4b, is due to thermal decomposition of brucite [39] with formation of MgO. Reaction (3) is due to dehydroxylation of antigorite [40,37,38]. In both samples, the DTG curves show two additional signals at about 625 and 735 °C that mark how the development of the dehydroxylation reaction occurs in multiple steps [41-44]. The 625 °C thermal event is due to the removal of adjacent hydroxyl groups that diffuse through the mineral structure with formation of a metastable phase [45-47]; the subsequent reaction (735 °C) leads to the complete dehydroxylation of antigorite and the beginning of the transformation to forsterite. Nevertheless, the interpretation of the dehydroxylation reaction through a multi-step mechanism with the formation of one or more metastable phases has recently been proposed [48]: these multiple thermal events could only be a consequence of isomorphic substitutions in octahedra or due to the occurrence of impurities, e.g., serpentine, a hypothesis also previously advanced by Viti [37]. Trickier is the interpretation of reaction (4), which could be ascribed to dehydroxylation of vermiculite or interlaminates [49,50], however, not identifiable through

XRPD.

The major difference between the two samples mainly concerns reaction (2) related to the thermal decomposition of brucite, which is less pronounced in the VG sample, in agreement with the QPA results that show a lower amount of brucite compared to the VV sample. As for antigorite, the small differences in the thermal range of occurrence and temperature of maximum reaction rate may be a consequence of structural/textural differences related to the origin of the two samples [51].

Micro-Raman data helped to confirm the identification of the phases in the serpentinites by comparison of the observed patterns with those available at the RRUFF Project database of Raman spectra, XRPD and chemistry data for minerals (*rruff.info/*). Fig. 5 reports examples of phases recognized in the VG serpentinite.

Specifically, antigorite (Fig. 5a) was identified on the basis of the major absorption bands at 143, 238, 386, 469, 536, 692, and 1053 nm, comparable with the bands reported in Rinaudo et al. [52] as far as the intensity and position are concerned. Awaruite (Fig. 5b) was identified on the basis of the major absorption bands at 113, 192, 203, 224, 310, 331, 352 cm^{-1} comparable with the bands reported in the RRUFF database and Chukanov, Vigasina [53]. Other minor phases that were not identified with other experimental techniques were also found: hematite (Fig. 5c) was recognised based on the major absorption bands at 225, 292, 410, and 612 cm^{-1} compared to those reported in the RRUFF database and de Faria, Lopes [54]. We observed antigorite, awaruite and hematite also for sample VV (see the examples of spectra as Supplementary Material Fig. 3S**)**.

SEM and EPMA analyses confirmed a wide chemical variability of major and minor mineral phases. Table 2a and Table 2b reports the averaged chemical data for the mineral phases of VG and VV, respectively.

SEM-EMPA analyses confirmed the results of XRPD analyses, while adding some insights on minor phases below the detection limit of XRPD. Figs. 6a and 6b show examples of Ni-bearing phases of VG and VV samples, while Table 2S of the Supplementary Material reports the chemical results for each analysed spot. Concerning the major phases, of both VG and VV, antigorite shows a slightly variable content of MgO (37.6–39.5 wt%) and SiO_2 (39.8–45.1 wt%), with a higher variability for minor elements such as Al_2O_3 (0.1–3.2 wt%), FeO (1.7–4.7 wt%), Cr_2O_3 (0–1.3), NiO (0–0.5), and minor content of CoO, CuO, TiO_2, MnO, and CaO (all below 0.1 wt%). In Fig. 6b, two different antigorite composition were detected, with *atg2* displaying a higher NiO (0.54 vs 0.13 wt%) content compared to *atg*. Olivine shows the prevalence of forsterite content, with MgO and FeO varying in the 49.3–54.6 wt% and 3.8–8.9 wt% range, respectively.

Minor elements are NiO (0.2–0.5 wt%), and MnO (0.2–0.4 wt%), with lower amount of CaO, TiO_2, CoO, and CuO (all below 0.1 wt%). As an example, in Fig. 6a, *ol1* has a higher FeO (6.77 vs 3.82 wt%) and NiO (0.31 vs 0.17 wt%) content with respect to *ol*. The pyroxene in both VV and VG samples is close to diopside end-member (MgO 16.9–18.6 wt%, CaO 24.7–26.8 wt%, FeO 0.5–1.9 wt%), with occasionally Al_2O_3 (0–2.1 wt%), Cr_2O_3 (0–1.0 wt%), and MnO, TiO_2, CuO (all below 0.1 wt %). Magnetite appears with an iron content in the 82.8–90.8 wt% range, with variable amounts of MgO (0.2–1.7 wt%), Cr_2O_3 (0–7.1 wt%), NiO (0–0.7 wt%), MnO (0.1–0.3 wt%), TiO_2 and CoO (both 0–0.2 wt%), and minor Al_2O_3, and CuO (all below 0.1 wt%) (see the Supplementary Material Table 2**S**). Brucite was detected by EPMA only in the VV sample, where substitutions of MgO with FeO (5.9–7.3 wt%), MnO (0.3–0.5 wt%), and minor CaO, CoO, and NiO (all below 0.1 wt%) were found.

Concerning the minor phases, SEM and EPMA analyses highlighted the presence of several Ni-bearing sulphides and alloys. The stoichiometry of these phases, as calculated from EPMA (see the Supplementary Material Table 2S), is not perfectly matching that found in the literature. A first group of sulphides, detected by EPMA in VV and only by SEM in VG, display a metal: sulphur proportion (M:S) close to 11:8, resembling that of pentlandite (M:S = 9:8), with one subgroup closer at

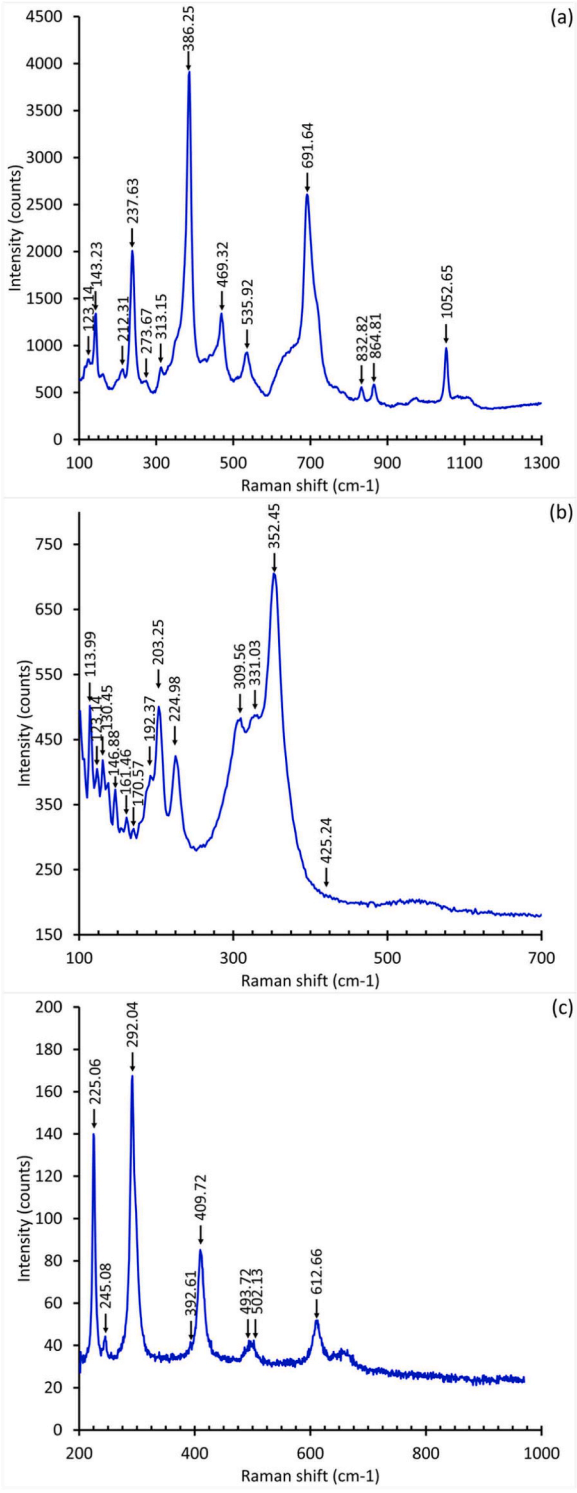

Fig. 5. Example of micro-Raman spectra of (a) antigorite, (b) awaruite; (c) hematite found in the VG sample. The same applies to the VV sample whose spectra are supplied as Supplementary Material Fig. 3S.

M:S= 9.4:8. In these sulphides, Fe:Ni is almost 1:1, but Co reach up to 1 atom per 8 S atoms. Another group of Fe-Ni sulphides display M:S= 3:2, typical of heazlewoodite (Ni_3S_2), but with almost Ni:Fe= 1:1 and minor cobalt (up to 0.3 atoms per 8 S). Ni-Fe alloys were detected in the VV sample with minor Cu and Co content. The Ni:Fe is 2.9:1.1, close to the 3:1 ratio of awaruite, while Cu and Co are in a concentration of 0.2 and 1.1 atoms %.

Table 2a
Chemical data of mineral phases of serpentinite "Verde Giada" (VG). hzl: heazlewoodite; mgn: magnetite; cpx: clinopyroxene (diopside); atg: antigorite; ol: olivine (forsterite).

Oxide (wt%)	hzl[#]	mgn	cpx	atg	ol
MgO		1.55	18.26	38.63	51.13
Al_2O_3				2.00	
SO_3	22.84[#]				
MnO		0.21			0.29
CaO			26.61		
SiO_2			54.83	42.60	40.97
TiO_2		0.19			
FeO	0.39[#]	28.49	0.67	2.53	6.68
Fe_2O_3[*]		66.29			
Cr_2O_3		2.62		0.36	
CoO	0.15[#]	0.18			
NiO	76.62[#]	0.46		0.09	0.34
CuO					
H_2O				13.70	0.47
Total	100.00	100.00	100.36	99.90	99.89
Atom (%)	**hzl**	**mgn**	**cpx**	**atg**	**ol**
Mg		1.26	9.82	14.73	26.50
Al				0.60	
S	35.14				
Mn		0.10			0.09
Ca			10.29		
Si			19.79	10.89	14.25
Ti		0.08			
Fe^{2+}	0.35	12.95	0.20	0.54	1.94
Fe^{3+}[*]		27.11			
Cr		1.13		0.07	
Co	0.12	0.08			
Ni	64.39	0.20		0.02	0.10
Cu					
O		57.10	59.89	49.77	57.12
H				23.37	
Total	100.00	100.00	100.00	100.00	100.00

wt% data refer to cation wt% of the corresponding oxide.
[*] Fe^{3+} calculated by Droop method for magnetite [55];

SEM analysis of filters highlighted, especially in the VV sample, the presence of chrysotile fibres (Fig. 7) which, however, were not detected during EPMA on polished resin-embedded specimens. This may indicate, as already stated, that chrysotile is not widespread in the rock (e.g. [7]) but local concentrations may be spread during crushing operations.

Fig. 8 reports three selected Ni-containing phases (magnetite in (a), antigorite in (b), and heazlewoodite in (c)) found during the TEM experimental session. The images are collected in HAADF and BF-STEM mode and the assemblages show the maps of the elements characteristic of each mineral. It is possible to note that magnetite (a) shows a homogeneous distribution of O, Fe, Cr, and minor Ni. Similarly, the analysed antigorite crystal shows, in addition to Mg, Si, and O, an enrichment of Ni. Finally, heazlewoodite is shown in (c) as a small crystal with high concentration of Ni and S, associated to other compounds with higher Mg, and Fe (probably antigorite and magnetite).

With all these data, following the flow chart reported in Fig. 3, the full mineralogical and chemical characterization of the Ni-bearing minerals present in the samples (Ni-containing mineralogy) is obtained. The calculated chemical formula for each mineral phase from the EPMA data than allows the calculation of the content of Ni in each mineral phase necessary for the next step of quantification of the Ni-containing phases using SEM/EDS.

3.3. Quantitative SEM analyses

We have determined the content of Ni-bearing minerals present in the samples using the quantitative SEM analysis used for the determination of asbestos minerals in massive samples, according with Italian Minister Decree September 6, 1994 [27]. With these numbers, it is possible to calculate the content of Ni of each mineral phase and consequently the Ni total content of the sample (the sum of each single contribution).

Starting from the results of the mineralogical characterization, we are aware that (i) amphiboles, chrysotile, ilmenite, and spinel/chromite may contain Ni; (ii) according to a recent study [2], Ni present in Valmalenco serpentine samples is mainly contained in the crystal lattice of antigorite; (iii) small amounts of Ni may be found in brucite, magnetite, and olivine found in our samples.

Regarding the quantification of Ni in each mineral species, the SEM analysis of filter mounts of VG and VV samples enabled to quantify Ni-bearing alloys and sulphides, and thus the related Ni amount. The detected phases are heazlewoodite and pentlandite in VG, and awaruite and pentlandite in VV.

Fig. 9a-f shows several examples of Ni-bearing minerals and their dimension as detected by SEM. As already described in the experimental Section 2.12, each individual of interest, after EDS measurement, was assimilated to a regular solid (mainly sphere and cylinder) on shape basis, allowing volume estimation. As an example, Fig. 9a shows a pentlandite grain (sample VG) with a volume of 29.5 μm^3, estimated as a cylinder with height of 5.170 μm and diameter of 2.698 μm. Similarly, Fig. 9d shows an awaruite crystal (sample VV) of 0.2 μm^3, assumed as a sphere of 0.741 μm in diameter.

In the 80 view fields explored for each sample (an area of ca. 1 mm^2), in VG and VV were detected 19 and 11 Ni-bearing phases, respectively (see Supplementary Material Table 3S**-a,b**). The total estimated volume of pentlandite was 30 μm^3 and 33 μm^3 for VG and VV, respectively. Concerning heazlewoodite, the total estimated volume was 136 μm^3 in the VG sample. Conversely, 54.3 μm^3 of awaruite were quantified in the only VV. Considering this estimation of alloys and sulphides' volumes and their chemical composition by EPMA, the Ni content sums up to 830 mg/kg in VG and 470 mg/kg in VV.

EPMA highlighted a low amount of Ni in most major phases such as antigorite (630 and 1060 mg/kg in VG and VV, respectively), olivine (2420 and 3180 mg/kg in VG and VV, respectively), and magnetite (3450 and 2710 mg/kg in VG and VV, respectively). These data indicate how Ni is widespread in almost all mineral phases of the Valmalenco serpentinites. Interestingly, however, the value of NiO in all the analysed pyroxenes was below detection limit, and in VV only one brucite aggregate was detected with 450 mg/kg of Ni, which is considered an exception. Considering these values and the results of the XRPD quantitative phase analysis (see Table 1b), the contribution of the major phases antigorite (73.3 and 72.8 wt% in VG and VV, respectively), olivine (22.4 and 13.1 wt% in VG and VV, respectively), and magnetite (2.6 and 3.8 wt% in VG and VV, respectively) to Ni content is 1094 mg/kg for VG and 1291 mg/kg for VV, respectively.

The total Ni content of the two samples is the sum of all the single contributions (see the flow chart in Fig. 3). Specifically, 830 + 1094 = 1924 mg/kg for VG and 470 + 1291 = 1761 mg/kg for VV. The values agree with the data of the bulk Ni content of VG and VV samples by ICP-MS analyses of 1500–1750 mg/kg for VG and 1390–1620 mg/kg for VV.

3.4. Nature of Ni and minerogenesis

To understand the stability of the mineralogical phases as a function of P-T-X conditions in the prograde metamorphism of ultramafic rocks, the study of metallic (ore) minerals is of crucial importance. Trommsdorff and Evans [56] recognized the magnetite, ilmenite, and pyrrhotite suite; Ni sulphides are also recognized, such as heazlewoodite (Ni_3S_2), pentlandite $(Fe,Ni)_9S_8$ and late awaruite (Ni_3Fe). Peretti [57] and Peretti et al. [58] show three main metamorphic assemblages of ore minerals, listed by increasing grade:

1. pentlandite - heazlewoodite - magnetite;.
2. pentlandite - awaruite - magnetite;.
3. heazlewoodite - awaruite - magnetite.

Each assemblage is constrained by the ratio $f(O_2)/f(S_2)$, for a definite

Table 2b
Chemical data of mineral phases of serpentinite "Verde Vittoria" (VV). awr: awaruite; pnt: pentlandite; mgn: magnetite; cpx: clinopyroxene (diopside); atg: antigorite; ol: olivine (forsterite); brc: brucite.

Oxide (wt%)	awr#	pnt#	mgn	cpx	atg	ol	brc
MgO		0.03#	0.75	17.85	38.33	49.79	63.60
Al_2O_3					1.44		
SO_3		32.27#					
MnO			0.26			0.27	0.39
CaO				26.68			
SiO_2		0.02#		55.75	43.62	40.84	
TiO_2			0.16				
FeO	25.62#	32.94#	29.87	0.90	3.17	8.78	6.60
Fe_2O_3*			63.12				
Cr_2O_3			5.32		0.37		
CoO	1.15#	5.03#					
NiO	73.06#	29.71#	0.52		0.14	0.40	
CuO	0.17#						
H_2O					12.82		29.25
Total	100.00	100.00	100.00	101.18	99.89	100.08	99.84
Atoms (%)	awr	pnt	mgn	cpx	atg	ol	brc
Mg		0.05	0.61	9.53	14.88	25.89	19.19
Al					0.44		
S		45.95					
Mn			0.12			0.08	0.07
Ca				10.24			
Si		0.04		19.97	11.36	14.24	
Ti			0.07				
Fe^{2+}	26.58	26.94	13.64	0.27	0.69	2.56	1.12
Fe^{3+}*			25.94				
Cr			2.30		0.08		
Co	1.13	3.90					
Ni	72.13	23.12	0.23		0.03	0.11	
Cu	0.16						
O			57.09	59.99	50.24	57.12	40.13
H					22.28		39.50
Total	100.00	100.00	100.00	100.00	100.00	100.00	100.00

wt% data refer to cation wt% of the corresponding oxide.
* Fe^{3+} calculated by Droop method for magnetite [55];

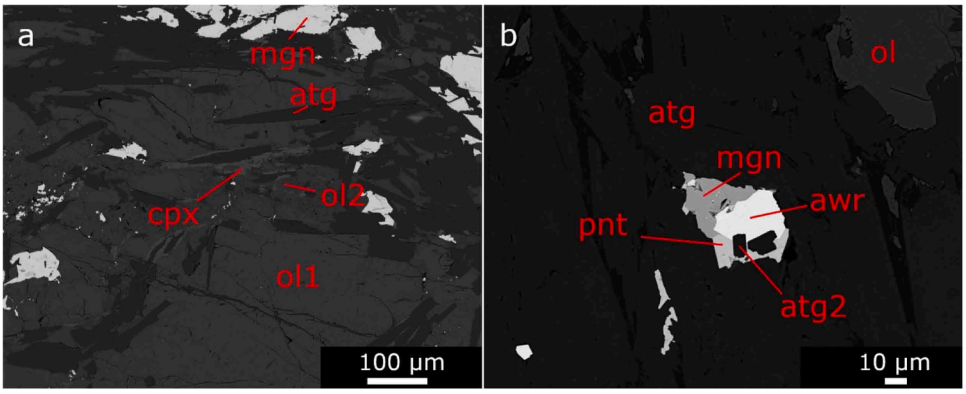

Fig. 6. EPMA images of VG (a) and VV (b) samples. ol-ol1: olivine (forsterite); atg: antigorite; cpx: clinopyroxene (diopside); mgn: magnetite; awr: awaruite; pnt: pentlandite.

P-T interval; the assemblage that forms under the most reducing conditions is pentlandite - awaruite - magnetite, and the strongly reducing conditions are confirmed by the presence of native copper in samples exhibiting the pentlandite - awaruite - magnetite and heazlewoodite - awaruite - magnetite assemblages [58]. The awaruite-in isograd coincides in serpentinite approximately with the olivine-in isograd; studies of fluid inclusions in the diopside indicate highly reducing conditions, with $f(O_2)$ values less than 4 log units below the quartz-fayalite-magnetite (QFM) buffer and H_2 contents of about 1 mol. %, as evidenced by micro-Raman analyses [58]. The highly reducing fluids are believed to have formed both during serpentinisation and de-serpentinisation, at the olivine-in isograd. These genetic conditions are therefore not compatible with the stability of bunsenite NiO [59,60], with no evidence in the Valmalenco serpentinites, even in the late stages with the formation of talc and chrysotile veins and lodes.

In VG and VV, the occurrence of heazlewoodite and awaruite may indicate reducing conditions with variable sulphur fugacity in the system, possibly excluding the presence of bunsenite [61].

3.5. *Implications for the health hazards and legislation issues*

The results of this study confirmed that Ni occurs in the products of the Italian Valmalenco "massive" serpentinite quarries of "Verde Vittoria" (VV) and "Verde Giada" (VG) and consequently in the quarry

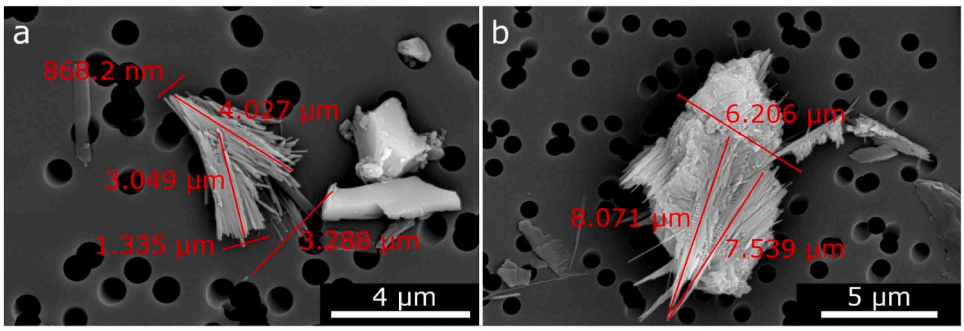

Fig. 7. SEM images of chrysotile fibres occurring in the VV sample filter mount.

wastes. We have found that Ni is mostly occluded inside the crystal lattice of the major crystalline phases of the serpentinites (antigorite, olivine, magnetite and brucite) with 1094 mg/kg for VG sample and 1291 mg/kg for VV sample, respectively. The carcinogenic mineral phase NiO (bunsenite) was not detected but we have determined a Ni content associated to the minor sulphides pentlandite, heazlewoodite and the natural alloy awaruite of 830 mg/kg for VG sample and 470 mg/kg for VV sample, respectively. According to the International Agency for Research on Cancer [62], "*There is sufficient evidence in humans for the carcinogenicity of mixtures that include nickel compounds and these agents cause cancers of the lung and of the nasal cavity and paranasal sinuses*". The carcinogenicity of trace metals like Ni has been reviewed by Boffetta [63] and recently by Schaumlöffel [64]. It depends mainly on oxidation states and crystal-chemistry of the Ni-compounds with complexes formed in vivo, in the vicinity of DNA, that catalyse redox reactions which in turn may oxidize and cause alteration of DNA [65]. Although these compounds are regarded as carcinogenic substances, there are inconsistencies among results on carcinogenicity of water-soluble Ni compounds. For example, Goodman et al. [66] found limited epidemiological evidence for increased cancer risk in the presence of certain forms of insoluble nickel and limited evidence that suggests they may act as a tumour promoter.

We have confirmed that these natural products contain rare chrysotile bundles as already reported by Cavallo [5], but no amphibole asbestos, like fibrous tremolite, were detected. The presence of chrysotile does not prevent the mining of these natural materials that must follow the regulations reported in the Appendix 4 "Criteria for the classification and use of green stones according to their content of asbestos" (in Italian) of the Law by decree of the Italian Ministry of Health [67], Art. 4. For each asbestos containing green stone mining site, mining operations must include [68]: (1) a geological survey of the deposit; (2) a suitable mining operation plan; (3) a safety plan with measures to decrease the risk of exposure to asbestos for the workers; (4) safety and professional training of the workers; (5) monitoring of the asbestos concentration in the *tout-venant* with optical (polarized light, PLOM, and phase-contrast, PCOM, optical microscopy) and electron microscopy (SEM); (6) certification of the product based on the concentration of asbestos and identification of the suitable use.

For the serpentine material extracted in the quarry, the Italian Health Ministerial Decree of May 14, 1996 evaluates the hazard due to the presence of asbestos by means of an "asbestos fibres' release index" to be measured in the case the serpentine material is extracted in brecciated matrix, in blocks for embankments or in ornamental slabs. This procedure with the "asbestos fibres' release index" is a derogation from the Italian Law No. 257 (March 27, 1992) which prohibits mining and marketing of asbestos-containing products in Italy. No constraints are set for the Ni contamination.

For cases other than the serpentine material extracted in the quarry, asbestos and Ni are considered sensitive parameters and are the materials are subjected to concentration limits. For example, a soil is considered to be polluted if asbestos exceeds 1000 mg/Kg, while for Ni the limit depends on the intended use of the site: 120 mg/kg for public/private/residential green areas, 500 mg/Kg for industrial/commercial areas. In the case of a mining waste, the situation is even more complicated. As anticipated in the introduction of this work, the determination of the nature of the phases that accommodate Ni is necessary to assess their toxicity and carcinogenicity potential. This is mandatory for the evaluation of the risks associated to that hazardous waste as individual substances have specific limits, classification and classes of risk if the detected concentrations exceed the relative limits provided by the existing regulations. Therefore, while for asbestos, classified IARC carcinogen of Group 1 a, competes a threshold value of 0.1 wt%, for Ni it is necessary to determine in what forms it is bound and to verify compliance with the limit for each different hazard class considered so to address the correct disposal action.

4. Conclusions

In this work, an analytical protocol is proposed for the identification and quantification of Ni in serpentinite rocks. The applied protocol proved to be reliable for both the case studies "Verde Giada" (VG) and "Verde Vittoria" (VV), two commercial varieties of massive serpentinite from Valmalenco (Sondrio, Central Italian Alps). The total Ni content computed as sum of each contribution from the Ni-containing minerals is 1924 and 1761 mg/kg for VG and VV, respectively, in good agreement with bulk ICP-MS analyses (1500–1750 mg/kg and 1390–1620 mg/kg for VG and VV, respectively).

The proposed protocol provides robust results: it is possible to obtain a detailed overview of the Ni speciation in a rock, commercial product, waste material, or environmental sample through a suite of routine techniques. The adopted protocol is of ease applicability for any laboratory dealing with environmental analysis, since it mostly mimics the conventional procedures adopted for asbestos. Moreover, the knowledge deriving from such analyses may be a support for the study of carcinogenicity and toxicity of Ni-bearing minerals. Indeed, knowledge on the toxicity/carcinogenicity of specific mineralogical species can be transferred to complex natural settings relying on the peculiar Ni speciation obtained from the protocol.

The procedure proposed for Ni could be expanded to include other metals like Cr and possibly other contaminants that share similar mineralogical occurrences. Future research efforts focusing on studying such elements by applying and potentially refining the protocol described here are promising and encouraged. This protocol could become a valuable resource for regulatory authorities, environmental laboratories, and research institutions.

Environmental implication

We focus on Ni compounds naturally occurring in serpentinites. Ni has several compounds that are regulated known carcinogen (e.g. bunsenite mineral, NiO). However, Ni also occurs as trace element in other minerals, which are not considered "hazardous material".

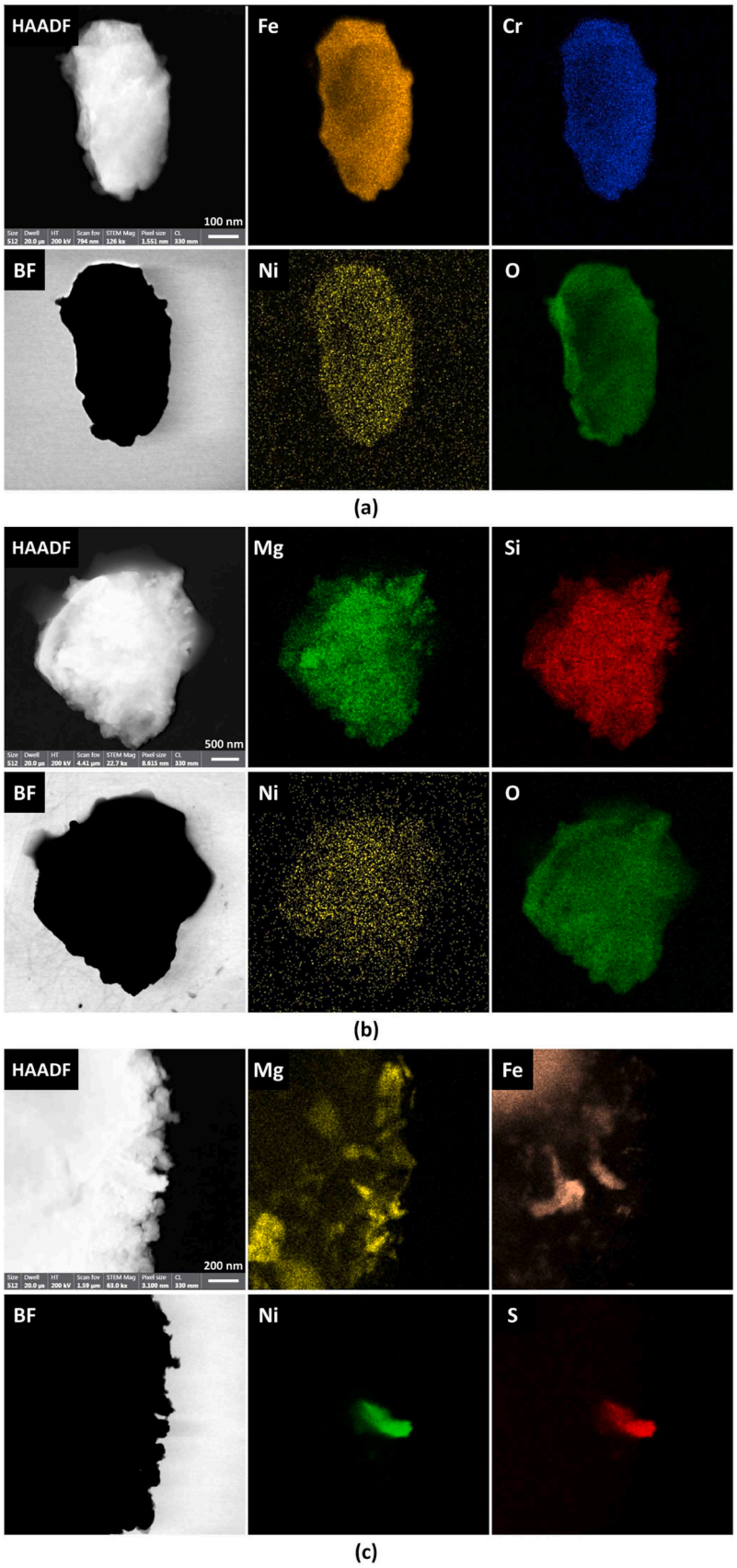

Fig. 8. Selected TEM images of three Ni-containing phases in HAADF and BF-STEM mode together with the maps of the characteristic elements of the minerals. (a) magnetite; (b) antigorite; (c) heazlewoodite. Analysis and images were performed at 200 KeV.

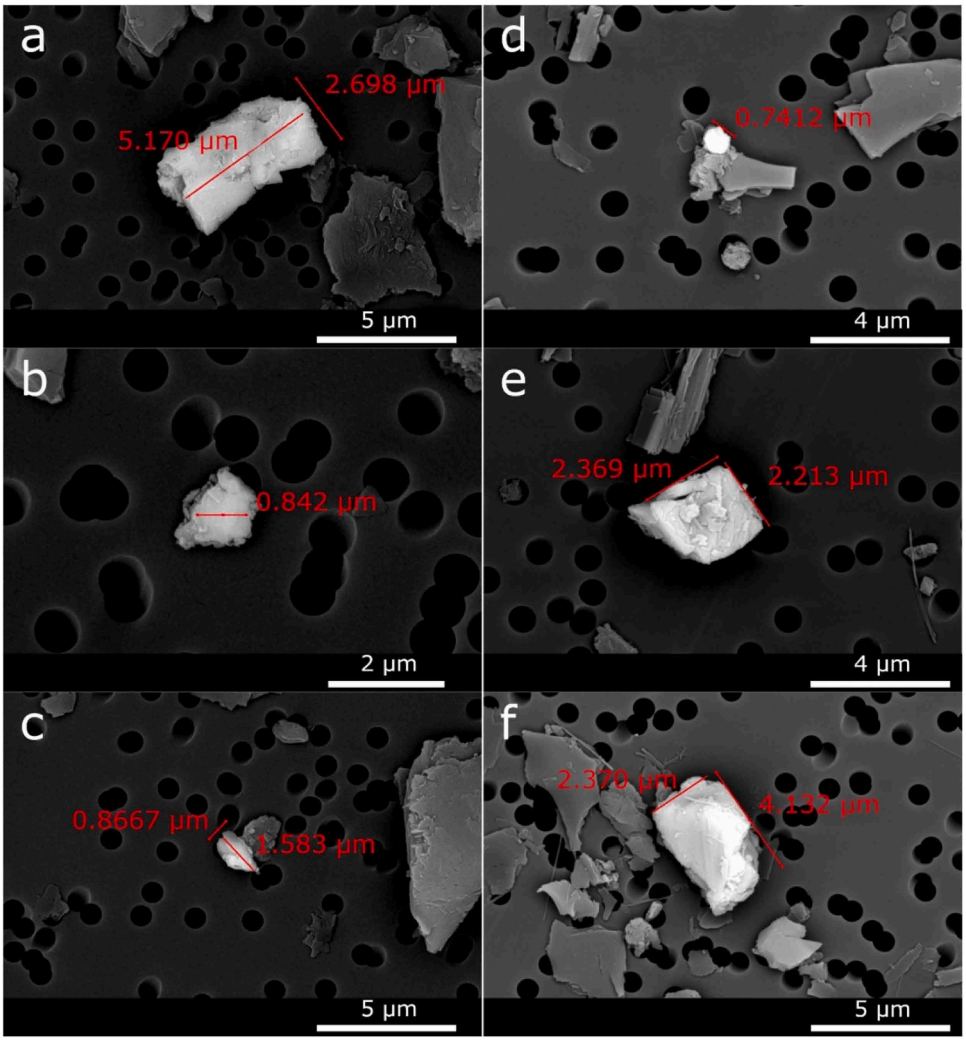

Fig. 9. SEM images of filter mounts of VG (a-c) and VV (d-f) samples. Red markers represent measurements performed on Ni-bearing minerals: a,c,e,f) cylindrical model; b,d) spherical model. Mineral phases: a,e,f) pentlandite; b-c) heazlewoodite; d) awaruite. Noteworthy, some mineral fibres are visible in figures e-f.

Environmental and social problems may arise when monitoring campaigns in serpentinite dressing plants employ bulk analytical techniques, which are not able to distinguish between diverse Ni occurrences. Our protocol enables to detect each hazardous phase, also distinguishing the contribution of non-hazardous minerals to the bulk Ni concentration. This method can be eventually applied to other contaminant metal species.

CRediT authorship contribution statement

Filippo Da Val: Methodology, Investigation, Conceptualization. **Alessandro Cavallo:** Writing – review & editing. **Maria Cristina Gamberini:** Investigation, Formal analysis, Data curation. **Mauro Zapparoli:** Investigation, Data curation. **Daniele Malferrari:** Writing – review & editing, Investigation, Formal analysis, Data curation. **Mattia Sisti:** Investigation, Data curation. **Rossella Arletti:** Writing – review & editing. **Riccardo Fantini:** Writing – review & editing, Investigation, Formal analysis, Data curation. **Alessandro Francesco Gualtieri:** Writing – original draft, Methodology, Investigation, Funding acquisition, Formal analysis, Data curation, Conceptualization.

Declaration of Competing Interest

The authors declare the following financial interests/personal relationships which may be considered as potential competing interests: Filippo Da Val reports a relationship with Consorzio Artigiani Cavatori S.R.L. Valrosera Sondrio (Italy) and SERPENTINO e GRANITI, Chiuro (Italy) that includes: consulting or advisory. Alessandro Cavallo (University of Milan, Italy) reports a relationship with Consorzio Artigiani Cavatori S.R.L. Valrosera Sondrio (Italy) and SERPENTINO e GRANITI, Chiuro (Italy) that includes: consulting or advisory. If there are other authors, they declare that they have no known competing financial interests or personal relationships that could have appeared to influence the work reported in this paper.

Data Availability

Data will be made available on request.

Acknowledgments

Funding: the work is supported by the Italian Ministry for Universities and Research (MUR, PRIN project “Fibres: a multidisciplinary mineralogical, crystal-chemical and biological project to amend the paradigm of toxicity and cancerogenicity of mineral fibres”—Bando 2017—Prot. 20173X8WA4). We acknowledge the Consorzio Artigiani Cavatori S.R.L. Valrosera Sondrio (Italy) and SERPENTINO e GRANITI, Chiuro (Italy) for providing the samples for this study. Andrea Risplendente is kindly acknowledged for the collection of the EPMA data at the Earth Sciences Department “Ardito Desio” of the University of Milan

(Italy). Finally, authors warmly thank the editor and reviewers for their suggestion and support during revision.

Appendix A. Supporting information

Supplementary data associated with this article can be found in the online version at doi:10.1016/j.jhazmat.2024.134928.

References

[1] Coleman, R.G., 1977. What is an Ophiolite?. In: Ophiolites. Minerals and Rocks, 12 Springer,, Berlin, Heidelberg, pp. 1–7. https://doi.org/10.1007/978-3-642-66673-5_1.

[2] Cavallo, A., 2022. Serpentino della Valmalenco" (Central Alps, Northern Italy): a green dimension stone with outstanding properties. Res Policy 75, 102467. https://doi.org/10.1016/j.resourpol.2021.102467.

[3] O'Hanley, D.S., 1996. Serpentinites: records of tectonic and petrological history. Oxford University Press,, New York, p. 277.

[4] Pereira, D., Blanco, J.A., Peinado, M., 2013. Study on serpentinites and the consequence of the misuse of natural stone in buildings for construction. J Mat Civ Eng 25 (10), 1563–1567. https://doi.org/10.1061/(ASCE)MT.1943-5533.0000689.

[5] Cavallo, A., 2018. Serpentinitic waste materials from the dimension stone industry: characterization, possible reuses and critical issues. Resour Pol 59, 17–23. https://doi.org/10.1016/j.resourpol.2018.08.003.

[6] Cattaneo, A., Somigliana, A., Gemmi, M., Bernabeo, F., Savoca, D., Cavallo, D.M., Bertazzi, P.A., 2012. Airborne concentrations of chrysotile asbestos in serpentine quarries and stone processing facilities in Valmalenco, Italy. Ann Occ Hyg 56 (6), 671–683. https://doi.org/10.1093/annhyg/mer119.

[7] Cavallo, A., Rimoldi, B., 2013. Chrysotile asbestos in serpentinite quarries: a case study in Valmalenco, Central Alps, Northern Italy. Env Sci: Process Impacts 15 (7), 1341–1350. https://doi.org/10.1039/C3EM00193H.

[8] Zucchetti, S., 1970. Ferro-nichel nativo ed altri minerali nicheliferi in serpentiniti anche asbestifere delle Alpi Occidentali. In: Rend. Soc. It. Mineral. Petrol, 26, pp. 377–397.

[9] Cavallo, A., 2020. Environmental asbestos contamination in an abandoned chrysotile mining site: the example of Val Malenco (central Alps, northern Italy). Epis J Int Geosci 43 (3), 851–858. https://doi.org/10.18814/epiiugs/2020/0200s01.

[10] Jacques, O., Pienitz, R., 2023. Limnological history of three lakes from the former asbestos mining region of Thetford Mines (southern Quebec, Canada). Aquat Sci 85 (4), 89. https://doi.org/10.1007/s00027-023-00985-5.

[11] Moore, T.R., Zimmermann, R.C., 1977. Establishment of vegetation on serpentine asbestos mine wastes, Southeastern Quebec Canada. J Appl Ecol 14, 589–599. https://doi.org/10.2307/2402569.

[12] Slavik, C.E., Demers, P.A., Tamburic, L., Warden, H., McLeod, C., 2023. Do patterns of past asbestos use and production reflect current geographic variations of cancer risk? Mesothelioma in Ontario and British Columbia, Canada. Cancer Causes Control 34 (4), 349–360. https://doi.org/10.1007/s10552-023-01672-4.

[13] Punturo, R., Ricchiuti, C., Giorno, E., Apollaro, C., Miriello, D., Visalli, R., Bloise, A., Pinizzotto, M.R., Cantaro, C., 2023. Potentially toxic elements (PTES) in actinolite and serpentinite host rocks: a case study from the Basilicata Region (Italy). Ofioliti 48 (2). https://doi.org/10.4454/ofioliti.v48i2.563.

[14] Shaheen, S.M., Chen, H.Y., Song, H., Rinklebe, J., Hseu, Z.Y., 2022. Release and mobilization of Ni, Co, and Cr under dynamic redox changes in a geogenic contaminated soil: assessing the potential risk in serpentine paddy environments. Sci Total Environ 850, 158087. https://doi.org/10.1016/j.scitotenv.2022.158087.

[15] Tashakor, M., Zuhairi Wan Yaacob, W., Mohamad, H., Abdul Ghani, A., Saadati, N., 2014. Assessment of selected sequential extraction and the toxicity characteristic leaching test as indices of metal mobility in serpentinite soils. Chem Speciat Bioavailab 26 (3), 139–147. https://doi.org/10.3184/095422914X14036277112433.

[16] Petriglieri, J.R., Barale, L., Viti, C., Ballirano, P., Belluso, E., Bruno, M.R., Campopiano, A., Cannizzaro, A., Fantauzzi, M., Gianchiglia, F., Montereali, M.R., Nardi, E., Olori, A., Piana, F., Tomatis, M., Rossi, A., Skogby, H., Pacella, A., Turci, F., 2023. From field analysis to nanostructural investigation: a multidisciplinary approach to describe natural occurrence of asbestos in view of hazard assessment. J Hazard Mater 457, 131754. https://doi.org/10.1016/j.jhazmat.2023.131754.

[17] Ricchiuti, C., Bloise, A., Punturo, R., 2020. Occurrence of asbestos in soils: state of the Art. Epis J Int Geosci 43 (3), 881–891.

[18] Hseu, Z.Y., 2018. Biogeochemistry of Serpentine Soils. Nova Science Pub Inc,, New York.

[19] Lago-Vila, M., Arenas-Lago, D., Rodríguez-Seijo, A., Andrade Couce, M.L., Vega, F. A., 2015. Cobalt, chromium and nickel contents in soils and plants from a serpentinite quarry. Solid earth 6 (1), 323–335. https://doi.org/10.5194/se-6-323-2015.

[20] Vithanage, M., Kumarathilaka, P., Oze, C., Suniti Karunatilake, M., Seneviratne, Z. Y., Hseu, V., Gunarathne, M., Dassanayake, Y., Sik, Ok, Rinklebe, J., 2019. Occurrence and cycling of trace elements in ultramafic soils and their impacts on human health: a critical review. Environ Int 131, 104974. https://doi.org/10.1016/j.envint.2019.104974.

[21] Bloise, A., Ricchiuti, C., Punturo, R., Pereira, D., 2020. Potentially toxic elements (PTEs) associated with asbestos chrysotile, tremolite and actinolite in the Calabria region (Italy). Chem Geol 558, 119896.

[22] Pereira, D., López, A.J., Ramil, A., Bloise, A., 2023. The importance of prevention when working with hazardous materials in the case of serpentinite and asbestos when cleaning monuments for restoration. Appl Sci 13 (1), 43.

[23] Trommsdorff, V., Montrasio, A., Hermann, J., Müntener, O., Spillmann, P., Gier, R., 2005. The geological map of Valmalenco. Schweiz Mineral und Petrogr Mitt 85, 1–13.

[24] Münterer, O., Hermann, J., Trommsdorff, V., 2000. Cooling history and exhumation of lower-crustal granulite and upper mantle (Malenco, eastern Central Alps). J Pet 41, 175–200. https://doi.org/10.1093/petrology/41.2.175.

[25] Müntener, O., Hermann, J., 1996. The Val Malenco lower crust-upper mantle complex and its field relations (Italian Alps). Schweiz Mineral Petrogr Mitt 76, 475–500.

[26] Trommsdorff, V., Piccardo, G.B., Montrasio, A., 1993. From magmatism through metamorphism to sea floor emplacement of subcontinental Adria lithosphere during pre-Alpine rifting (Malenco, Italy). Schweiz Mineral Petr Mitt 73, 191–203.

[27] Italian Ministry of Health, 1994. Normative e metodologie tecniche di applicazione dell'art.6, comma 3, e dell'art.12, comma 2, della legge 27 marzo 1992, n.257, relativa alla cessazione dell'impiego dell'amianto. GU Serie Generale n.220 del 20–09-1994 - Suppl. Ordinario n. 129. https://www.gazzettaufficiale.it/eli/id/1994/09/20/094A5917/sg (accessed 2023 Nov. 08).

[28] Larson, A.C., Von Dreele, R.B., 2004. General Structure Analysis System. Report LAUR 86–748. Los Alamos National Laboratory, New Mexico, USA.

[29] Toby, B.H., 2001. EXPGUI, a graphical user interface for GSAS. J Appl Cryst 34, 210–213. https://doi.org/10.1107/S0021889801002242.

[30] Dollase, W.A., 1986. Correction of intensities for preferred orientation in powder diffractometry: application of the March model. J Appl Cryst 19 (4), 267–272. https://doi.org/10.1107/S0021889886089458.

[31] Militello, G.M., Sanguineti, E., Gonzàlez, A., Gaggero, L., 2020. Asbestos amphiboles: effects of comminution on tremolite and actinolite regulated and unregulated fibres. Epis J Int Geosci 43 (3), 909–918. https://doi.org/10.18814/epiiugs/2020/0200s09.

[32] Capitani, G., Mellini, M., 2004. The modulated crystal structure of antigorite: the m= 17 polysome. Am Min 89 (1), 147–158. https://doi.org/10.2138/am-2004-0117.

[33] Hofmeister, W., Platen, H.V., 1992. Crystal chemistry and atomic order in brucite-related double-layer structures. Crystallogr Rev 3 (1), 3–26. https://doi.org/10.1080/08893119208032964.

[34] Cameron, M., Sueno, S., Prewitt, C.T., Papike, J.J., 1973. High-temperature crystal chemistry of acmite, diopside, hedenbergite jadeite, spodumene and ureyite. Am Miner: J Earth Planet Mater 58 (7-8), 594–618.

[35] Yoshida, J., Iida, S., 1977. X-ray diffraction study on the low temperature phase of magnetite. J Phys Soc Jpn 42 (1), 230–237. https://doi.org/10.1143/JPSJ.42.230.

[36] Birle, J.D., Gibbs, G.V., Moore, P.B., Smith, J.V., 1968. Crystal structures of natural olivines. Am Miner: J Earth Planet Mater 53 (5-6), 807–824.

[37] Viti, C., 2010. Serpentine minerals discrimination by thermal analysis. Am Mineral 95 (4), 631–638. https://doi.org/10.2138/am.2010.3366.

[38] Zahid, S., Oskierski, H.C., Oluwoye, I., Brand, H.E.A., Xia, F., Senanayake, G., Altarawneh, M., Dlugogorski, B.Z., 2022. Kinetics of antigorite dehydroxylation for CO_2 sequestration. Miner Eng 184. https://doi.org/10.1016/j.mineng.2022.107630.

[39] Malferrari, D., Giuseppe, Di, Scognamiglio, D., Gualtieri, A.F, V., 2021. Commercial brucite, a worldwide used raw material deemed safe, can be contaminated by asbestos. Period di Mineral 90 (3), 317–324 https://doi.org/10.13133/2239-1002/17384.

[40] Gualtieri, A.F., Giacobbe, C., Viti, C., 2012. The dehydroxylation of serpentine group minerals. Am Mineral 97 (4), 666–680. https://doi.org/10.2138/am.2012.3952.

[41] Ball, M.C., Taylor, H.F.W., 1963. The dehydration of chrysotile in air and under hydrothermal conditions. Mineral Mag 33, 467–482. https://doi.org/10.1180/minmag.1963.033.261.04.

[42] Brindley, G.W., Hayami, R., 1965. Mechanism of formation of forsterite and enstatite from serpentine. Mineral Mag 35, 189–195. https://doi.org/10.1180/minmag.1965.035.269.21.

[43] MacKenzie, K.J.D., Meinhold, R.H., 1994. Thermal reactions of chrysotile revised: A 29Si and 25Mg MAS NMR study. American Mineralogist, 79, 43–50. ISSN: 1945–3027.

[44] Martin, C.J., 1977. The thermal decomposition of chrysotile. Mineral Mag 41, 453–459. https://doi.org/10.1180/minmag.1977.041.320.05.

[45] Trittschack, R., Grobēty, B., 2012. Dehydroxylation kinetics of lizardite. Eur J Mineral 24 (1), 47–57. https://doi.org/10.1127/0935-1221/2012/0024-2169.

[46] Trittschack, R., Grobēty, B., Brodard, P., 2014. Kinetics of the chrysotile and brucite dehydroxylation reaction: a combined non-isothermal/isothermal thermogravimetric analysis and high-temperature X-ray powder diffraction study. Phys Chem Miner 41 (3), 197–214. https://doi.org/10.1007/s00269-013-0638-9.

[47] Wang, D., Liu, X., Liu, T., Shen, K., Welch, D.O., Li, B., 2017. Constraints from the dehydration of antigorite on high-conductivity anomalies in subduction zones. Sci Rep 7 (1), 16893. https://doi.org/10.1038/s41598-017-16883-4.

[48] Ferrand, T.P., 2019. Neither antigorite nor its dehydration is "metastable". Am Mineral 104 (6), 788–790. https://doi.org/10.2138/am-2019-6957.

[49] Földvári, M., 2013. Handbook of thermogravimetric system of minerals and its use in geological practice. Geol Inst Hung 180, p.

[50] Kresten, P., Berggren, G., 1978. The thermal decomposition of vermiculite. Thermochim Acta 23 (1), 171–182. https://doi.org/10.1016/0040-6031(78)85123-5.
[51] Perez-Rodriguez, J.L., Franco, F., Ramirez-Valle, V., Perez-Maqueda, L.A., 2005. Modification of the thermal dehydroxylation of antigorite by ultrasound treatment. J Therm Anal Calorim 82, 769–774. https://doi.org/10.1007/s10973-005-0962-5.
[52] Rinaudo, C., Gastaldi, D., Belluso, E., 2003. Characterization of chrysotile, antigorite and lizardite by FT-Raman spectroscopy. Can Mineral 41 (4), 883–890. https://doi.org/10.2113/gscanmin.41.4.883.
[53] Chukanov, N.V., Vigasina, M.F., 2020. Raman spectra of minerals. Vibrational (Infrared and Raman) Spectra of Minerals and Related Compounds. Springer Mineralogy. Springer,, Cham. https://doi.org/10.1007/978-3-030-26803-9_4.
[54] de Faria, D.L.A., Lopes, F.N., 2007. Heated goethite and natural hematite: can Raman spectroscopy be used to differentiate them? Vib Spectrosc 45 (2), 117–121. https://doi.org/10.1016/j.vibspec.2007.07.003.
[55] Droop, G.T.R., 1987. A general equation for estimating Fe3+ concentrations in ferromagnesian silicates and oxides from microprobe analyses, using stoichiometric criteria. Mineral Mag 51 (361), 431–435. https://doi.org/10.1180/minmag.1987.051.361.10.
[56] Trommsdorff, V., Evans, B.W., 1974. Alpine metamorphism of peridotitic rocks. Schweiz Mineral Petrogr Mitt 54, 333–352.
[57] Peretti, A. 1988. Occurrence and stabilities of opaque minerals in the Malenco serpentinite (Sondrio, Northern Italy). Ph. D. Thesis ETH Zürich.
[58] Peretti, A., Dubessy, J., Mullis, J., Frost, B.R., Trommsdorff, V., 1992. Highly reducing conditions during Alpine metamorphism of the Malenco peridotite (Sondrio, northern Italy) indicated by mineral paragenesis and H_2 in fluid inclusions. Contrib Mineral Petrol 112, 329–340. https://doi.org/10.1007/BF00310464.
[59] Hemingway, B.S., 1990. Thermodynamic properties for bunsenite, NiO, magnetite, Fe_3O_4, and hematite, Fe_2O_3, with comments on selected oxygen buffer reactions. Am Mineral 75 (7-8), 781–790.
[60] Ludwig, C., Casey, W.H., 1996. On the mechanisms of dissolution of bunsenite [NiO(s)] and other simple oxide minerals. J Colloid Interface Sci 178 (1), 176–185. https://doi.org/10.1006/jcis.1996.0106.
[61] Klein, F., Bach, W., 2009. Fe–Ni–Co–O–S phase relations in peridotite–seawater interactions. J Petrol 50 (1), 37–59.
[62] International Agency for Research on Cancer, 1990. IARC Monographs on the Evaluation of the Carcinogenic Risk of Chemicals to Man. Chromium, Nickel, and Welding. Vol. 49. Lyon, France: IARC, pp. 677.
[63] Boffetta, P., 1993. Carcinogenicity of trace elements with reference to evaluations made by the International Agency for Research on Cancer. Scand J Work, Environ Health 19 (1), 67–70.
[64] Schaumlöffel, D., 2012. Nickel species: analysis and toxic effects. J Trace Elem Med Biol 26 (1), 1–6. https://doi.org/10.1016/j.jtemb.2012.01.002.
[65] Mulware, S.J., 2013. Trace elements and carcinogenicity: a subject in review. Biotech 3, 85–96. https://doi.org/10.1007/s13205-012-0072-6.
[66] Goodman, J.E., Prueitt, R.L., Dodge, D.G., Thakali, S., 2009. Carcinogenicity assessment of water-soluble nickel compounds. Crit Rev Toxicol 39 (5), 365–417. https://doi.org/10.1080/10408440902762777.
[67] Italian Ministry of Health, 1996. Normative e metodologie tecniche per gli interventi di bonifica, ivi compresi quelli per rendere innocuo l'amianto, previsti dall'art. 5, comma 1, lettera f), della legge 27 marzo 1992, n. 257, recante: "Norme relative alla cessazione dell'impiego dell'amianto", GU Serie Generale n.251 del 25–10-1996 - Suppl. Ordinario n. 178. https://www.gazzettaufficiale.it/eli/id/1996/10/25/096A6000/sg (accessed 2023 Nov. 08).
[68] Gualtieri, A.F., Gandolfi, N.B., Pollastri, S., Rinaldi, R., Sala, O., Martinelli, G., Bacci, T., Paoli, F., Viani, A., Vigliaturo, R., 2018. Assessment of the potential hazard represented by natural raw materials containing mineral fibres—the case of the feldspar from Orani, Sardinia (Italy). J Hazard Mater 350, 76–87. https://doi.org/10.1016/j.jhazmat.2018.02.012.